



저작자표시 2.0 대한민국

이용자는 아래의 조건을 따르는 경우에 한하여 자유롭게

- 이 저작물을 복제, 배포, 전송, 전시, 공연 및 방송할 수 있습니다.
- 이차적 저작물을 작성할 수 있습니다.
- 이 저작물을 영리 목적으로 이용할 수 있습니다.

다음과 같은 조건을 따라야 합니다:



저작자표시. 귀하는 원저작자를 표시하여야 합니다.

- 귀하는, 이 저작물의 재이용이나 배포의 경우, 이 저작물에 적용된 이용허락조건을 명확하게 나타내어야 합니다.
- 저작권자로부터 별도의 허가를 받으면 이러한 조건들은 적용되지 않습니다.

저작권법에 따른 이용자의 권리는 위의 내용에 의하여 영향을 받지 않습니다.

이것은 [이용허락규약\(Legal Code\)](#)을 이해하기 쉽게 요약한 것입니다.

[Disclaimer](#) 

Activated carbon nanofiber nanoparticles
incorporated electrospun polycaprolactone
scaffolds to promote fibroblast behaviors for
application to skin tissue engineering

Sangmun Choi

Department of Medicine

The Graduate School, Yonsei University

Activated carbon nanofiber nanoparticles
incorporated electrospun polycaprolactone
scaffolds to promote fibroblast behaviors for
application to skin tissue engineering

Directed by Professor Jong-Chul Park

Doctoral Dissertation
submitted to the Department of Medicine,
the Graduate School of Yonsei University
in partial fulfillment of the requirements for the degree of
Doctor of Philosophy in Medical Science

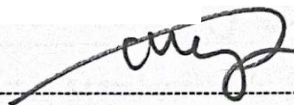
Sangmun Choi

December 2023

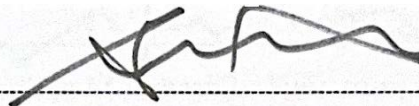
This certifies that the Doctoral Dissertation of
Sangmun Choi is approved.



Thesis Supervisor : Jong-Chul Park



Thesis Committee Member#1 : In Sik Yun



Thesis Committee Member#2 : Hak-Joon Sung



Thesis Committee Member#3 : Dong-Wook Han



Thesis Committee Member#4 : Young Sik Choi

The Graduate School
Yonsei University

December 2023

ACKNOWLEDGEMENTS

First and foremost, a special thanks to Prof. Jong-chul Park. Without his constant guidance, encouragement, and extensive knowledge, this thesis wouldn't have reached its completion. His dedication to his students and passion for the subject has made a profound impression on me.

I'd also like to extend my gratitude to Prof. Dong-Wook Han. His feedback and unique perspectives have always pushed me to think deeper and refine my work. His expertise was a beacon when I was lost in the vast research sea.

To my family, thank you for always being there. Your unwavering support, understanding, and love have been the backbone of my journey. You believed in me even when I doubted myself, and I am eternally grateful for that.

<TABLE OF CONTENTS>

ABSTRACT	iv
I. INTRODUCTION	1
II. MATERIALS AND METHODS	5
1. Preparation of electrospun PAN nanofiber and conversion into CNF and ACNF NPs	5
2. Preparation of ACNF@PCL and ACNF-PCL nanofiber mats	7
3. Bradford assay	8
4. In vitro cell culture experiments	9
5. Cell proliferation study	10
6. Statistical analysis	11
III. RESULTS and DISCUSSION	11
1. Physicochemical properties and cytotoxicity of CNF and ACNF NPs	11
2. Surface properties of ACNF@PCL and ACNF-PCL mats	21
3. Cell proliferation on ACNF@PCL and ACNF-PCL scaffolds	28
IV. CONCLUSION	32
REFERENCES	33
ABSTRACT (IN KOREAN)	38

LIST OF FIGURES

Figure 1-1. Electrospinning and self-deposition techniques in crafting ACNF-PCL composite mats: from polyacrylonitrile derivation to nanoparticle integration.	5
Figure 1-2. FTIR Analysis of PAN, CNF, and ACNF NPs with Emphasis on Wavenumber Shifts.	6
Figure 1-3. Preparation and Progression of ACNF@PCL Nanofiber Mats and Electrospun Composite Solutions.	7
Figure 2-1. SEM imaging of PAN, CNF, and ACNF mats: fiber diameters, nanoparticle structures, and Raman/XPS analysis.	13
Figure 2-2. FTIR Spectra Analysis of PAN, CNF, and ACNF NPs Highlighting Wavenumber Shifts.	14
Figure 2-3. BSA Optical Analysis and Protein Adsorption in CNF vs. ACNF.	16
Figure 2-4. ATR-FTIR Analysis of Electrospun PCL & ACNF-PCL Nanofiber Mats.	27
Figure 3-1. CNF and ACNF NPs' effects on NIH3T3 cells.	17
Figure 3-2. Microscopic Views of CNF/ACNF Treated NIH3T3 Cells over time.	18
Figure 3-3. Fluorescent Views of Cell Viability Post CNF/ACNF Treatment Over Time.	19
Figure 4-1. Wound healing assay with NIH3T3 cells.	19
Figure 4-2. Enlarged Microscopy of NP-Treated Cells in 24h Wound	

Healing Study.	21
Figure 5. Colloidal Stability & Visual Analysis of ACNF NPs in PBS & PCL-HFIP Solutions.	22
Figure 6. SEM and TEM imaging of ACNF@PCL and ACNF-PCL mats.	23
Figure 7. Wettability of PCL, ACNF@PCL, and ACNF-PCL nanofiber mats	25
Figure 8. Electrochemical analysis of PCL and ACNF-PCL mats. ...	26
Figure 9. CCK assay of cell proliferation on PCL and ACNF variants.	28
Figure 10. CLSM imaging of cell growth on PCL and ACNF scaffolds.	29
Figure 11-1. SEM visuals of cell proliferation on PCL and ACNF mats.	30
Figure 11-2. Cell Communication on PCL & ACNF Scaffolds: Day 3 SEM Insights.	30

ABSTRACT

Activated carbon nanofiber nanoparticles incorporated electrospun polycaprolactone scaffolds to promote fibroblast behaviors for application to skin tissue engineering

Sangmun Choi

*Department of Medicine
The Graduate School, Yonsei University*

(Directed by Professor Jong-Chul Park)

The most widely used one-dimensional (1D) carbonaceous nanomaterials in tissue engineering are carbon nanotubes, either single or multi-walled. Other forms of 1D nanomaterials, such as carbon nanowires and carbon nanofibers, have been less explored for biomedical applications. Herein, I synthesized 1D-activated carbon nanofiber nanoparticles (ACNF NPs) from the polyacrylonitrile electrospun nanofibers by continuous processes like stabilization, alkali treatment, calcination, and grinding. Two different sets of ACNF NPs-containing electrospun polycaprolactone (PCL) nanofiber mats, viz. surface-modified NP-deposited mats (ACNF@PCL) and NP-incorporated mats (ACNF-PCL), were prepared to examine their potential as skin tissue engineering scaffolds. Raman spectra demonstrated that ACNF NPs exhibited graphitization degree with an ID/IG ratio of 1.05.

Scanning electron microscopy (SEM) observations showed that ACNF NPs are sized 280 ± 100 nm by diameter and 565–3322 nm by length. The NPs concentrated above 30 $\mu\text{g/mL}$ were found to exhibit toxicity with $< 70\%$ viability of NIH3T3 fibroblasts at 48 h. The ACNF-PCL nanofiber mats displayed a better cell proliferation profile, showing significant changes compared to PCL and ACNF@PCL mats on days 1, 3, and 5. Hence, I concluded that ACNF-PCL mats with less concentration of ACNF NPs have more potential to support cellular growth, ensuring its possible impact on skin tissue regeneration.

Key words : electrospun nanofiber, activated carbon nanofiber nanoparticles, polycaprolactone, skin tissue engineering

Activated carbon nanofiber nanoparticles incorporated electrospun polycaprolactone scaffolds to promote fibroblast behaviors for application to skin tissue engineering

Sangmun Choi

*Department of Medicine
The Graduate School, Yonsei University*

(Directed by Professor Jong-Chul Park)

I. INTRODUCTION

Carbonaceous nanomaterials are the specialized candidates in biomedical fields, including drug delivery, bioimaging, antibacterial application, and tissue engineering¹. The nanomaterials exhibit massive structural diversities as the carbon atoms involve in covalent bonding at different hybridization states (sp, sp², and sp³)². The allotropes of carbon nanomaterials are classified into different dimensional nanostructures, i.e., 0D (ex. quantum dots), 1D (ex. carbon nanotubes), and 2D (ex. graphene nanosheets), and their electrical properties are highly influenced by the degree of replication³.

As far as 1D-carbon nanomaterials are concerned, carbon nanotubes (CNTs) (either single or multiwalled) are the well-explored nanomaterials as their nanocomposites in several biomedical applications, including tissue engineering⁴. But other 1D-carbon nanomaterials such as carbon nanofibers and carbon nanowires have been less studied for their biomedical applications. In the present work, I have prepared activated carbon nanofiber nanoparticles (ACNF NPs) from the electrospun polyacrylonitrile (PAN) nanofiber mats following subsequent experimental processes such as stabilization, alkali treatment, calcination, and

grinding.

And, I prepared two various types of electroactive nanofiber mats, i.e., ACNF@PCL by self-deposition of ACNF NPs over electrospun polycaprolactone (PCL) nanofiber mats and ACNF-PCL by electrospinning the composite of PCL and ACNF NPs. In each type, I varied the concentration of NPs to have different samples and provided comparative data in physicochemical and cell line experiments for the perspective application of skin tissue engineering.

When a wound appears on the skin, the transepithelial potential of epithelial cells is severely disturbed, causing a decrease in wound potential. As a result, a potential gradient is generated with a drive of positive charge flow from the surrounding healthy tissue to the damaged tissue⁵. As the effect induces directional migration of cells, the researchers presume that applying electroactive dressings at the wound site can be a promising approach healing the wound effectively.

Electrospun nanofiber mats are a kind of promising 3D wound healing scaffolds exhibiting air permeability, flexibility, drug encapsulation, wettability, and mechanical strength⁶. It is noteworthy that the nanofibers' surface properties can be tuned by the changes in solvent or polymeric composition, alteration in experimental parameters such as humidity, the distance between the needle and collector, and voltage, and various post-treatments to achieve effectiveness in tissue regeneration^{7,8}.

Carbon nanofibers are mainly synthesized by chemical vapor deposition (bottom-up) or electrospinning (top-down) techniques. The vapor-grown CNFs are produced up to 200 μm in length from the hydrocarbon gas using a catalytic growth process. They possess a stacking arrangement of graphene sheets with three established structural patterns: platelet, tubular, and herringbone⁹. Meanwhile, the electrospun CNFs are prepared from PAN polymer dissolved in dimethylformamide (DMF). Oxidative stabilization is necessary to

inherit the thermoset properties and preserve the structural integrity in PAN before the calcination process. These electrospun CNFs are continuous, highly pure, and less expensive, and can be prepared in large quantities with well-defined topologies. The hollow cavity in CNFs, as present in CNTs, can also be produced by processing the core-shell type PAN electrospun nanofibers¹⁰.

CNFs possess a high aspect ratio and low electrical resistivity. The tensile strength and tensile modulus of CNFs-containing polymeric composites have been estimated to be at least two orders of magnitude higher than that of neat polymers. For these reasons, CNFs are promising nano-filled thermosetting materials with high electrical conductivity for polymers. The CNFs can be adequate, inexpensive replacements for CNTs in developing high-performance resin formulations¹¹.

The researchers have revealed that electrospun non-woven carbon nanofiber mats have acted as the templates for anchoring photocatalysts like indium sulfide (In_2S_3) and formed hierarchical nanostructured heterojunction systems through the one-pot hydrothermal method. These CNF- In_2S_3 photocatalysts exhibited larger surface area, increased photo-induced charge separation, and enhanced light absorption, which allowed them to possess greater photocatalytic activity than pure In_2S_3 ¹².

However, the CNFs are not yet well explored for their photothermal and photodynamic properties though several research findings are available to demonstrate the same for other carbon nanomaterials, including CNTs and graphene¹³. Notably, the researchers have utilized different carbon nanomaterials for the combined photothermal and photodynamic treatments, like the transition metal dichalcogenides, pnictogens, MXene, graphitic carbon nitride, and boron nanosheets¹⁴. Though CNFs have been widely studied in cathodes, anodes, and supercapacitors for energy applications^{15,16}, their uses in tissue engineering are significantly less. However, there are some scientific reports to prove the potential of CNFs

in other kinds of tissue engineering, such as bone, muscle, and nerve¹⁷⁻¹⁹.

For decades, researchers have been developing functional electrospun nanofiber mats by incorporating bioactive molecules and nanoparticles for enhanced skin tissue engineering^{20,21}. For instance, silver nanoparticle-incorporated nanofiber scaffolds exhibited antimicrobial properties to fight against a broad spectrum of microbes at the wound site²². Copper-containing nanofiber scaffolds acted as wound dressing materials preventing biofilm formation on the wound site²³. Cerium oxide nanoparticle functionalized electrospun scaffolds have improved wound healing through their antioxidant properties²⁴. Under this context, carbon-based nanomaterials such as graphene oxide and carbon nanotubes are included to enhance the electrical property of the scaffolds²⁵. Some researchers have used them as fillers to increase the mechanical strength of nanofiber mats²⁶. Our work expects enhanced cell proliferation using NIH3T3 fibroblasts as the ACNF NP-based nanofiber mats are also electroactive.

A brief outline of the work, including synthesis of ACNF NPs and ACNF@PCL and ACNF-PCL mats and in vitro cell line studies, has been shown schematically in Figure 1-1. I anticipate that the comparative experimental data would determine the optimized concentrations of ACNF NPs in the scaffold, which can be considered for the in vivo skin tissue-engineering model.

II. MATERIALS AND METHODS

1. Preparation of electrospun PAN nanofiber and conversion into CNF and ACNF NPs

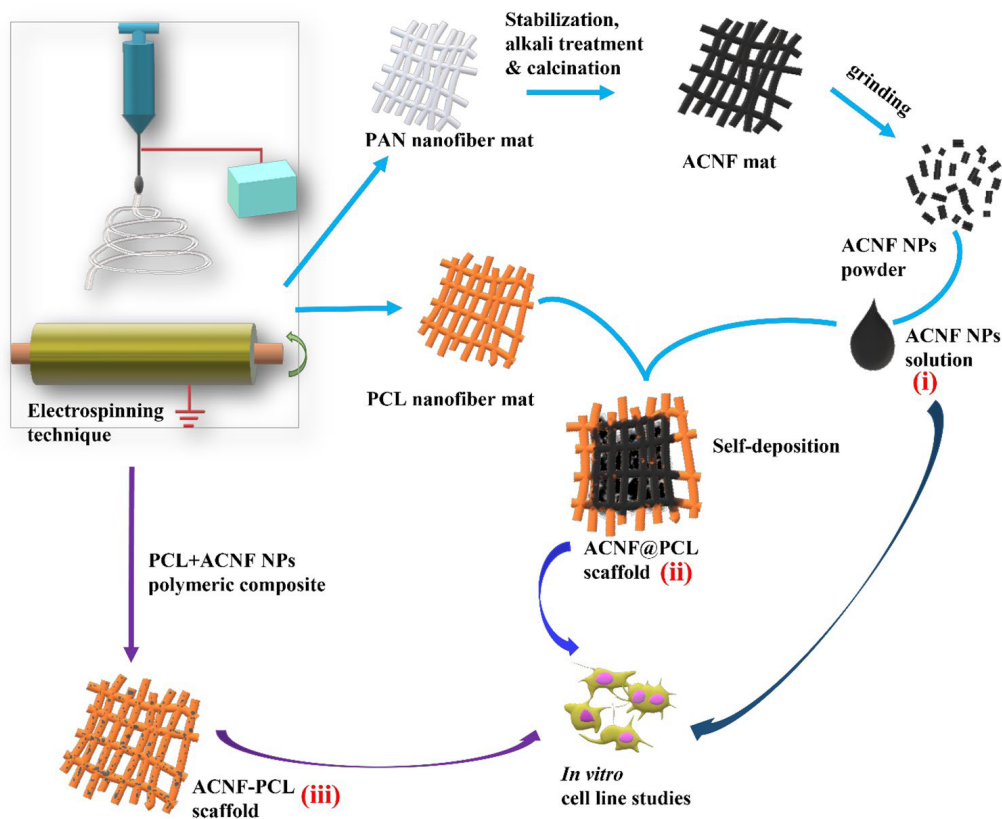


Figure 1-1. **a** Activated carbon nanofiber nanoparticles (ACNF NPs) obtained from electrospun polyacrylonitrile (PAN) nanofiber mat after stabilization, alkali treatment, calcination, and manual grinding. **b** Various ACNF@PCL mats prepared by self-deposition of ACNF NPs over the electrospun polycaprolactone (PCL) mat. **c** ACNF-PCL mats prepared by electrospinning the polymeric composite of PCL and ACNF NPs using different concentrations of NPs

A 10% (w/v) PAN solution was prepared by dissolving in DMF solvent under magnetic stirring for 4 h and taken into a 10-mL syringe fitted with a needle (inner diameter 0.5 mm). The distance between the needle and the aluminum foil collector on a cylindrical rotating drum was 10 cm. The speed of the rotating drum was set to 1000 rpm, and the applied voltage was 15 kV. The feeding rate of the solution was maintained at 0.8 mL/h during the

electrospinning process. The relative humidity and temperature of the chamber were maintained to be 35% and 25°C, respectively.

The as-prepared electrospun nanofiber mats were stabilized by heating in an air atmosphere for 2 h at 280°C with a heating rate of 1 °C/min. The stabilized mat was soaked in KOH solution (6 M) for 6 h, and subsequently, the calcination treatment was followed at 800°C for 1 h with a heating rate of 5 °C/min. The obtained ACNF mat was washed using acetone to remove the impurities and then treated with 1 N HCl to decrease the pH to 7.0. Then, the mat was dried in a hot air oven at 80°C for 12 h²⁷. Then, the nanofiber mat was crushed into powder manually using a pestle and mortar to obtain ACNF NPs for characterizations.

I prepared CNF NPs, also skipping the alkali treatment in the above experimental procedures and characterized them to compare with ACNF NPs. I have shown digital images of as-prepared PAN electrospun nanofiber mat, stabilized PAN, calcined CNF and ACNF, and the powdered samples in Figure 1-2.

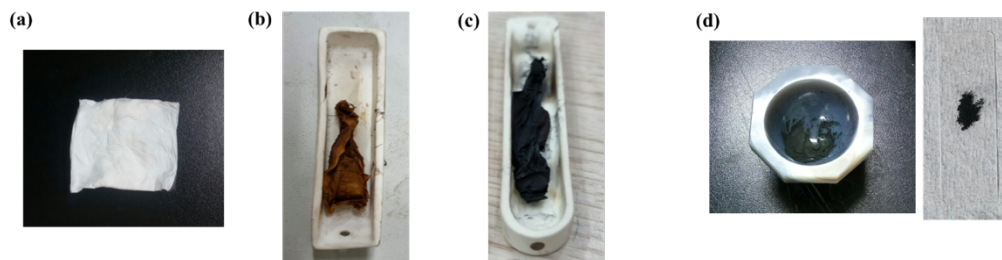


Figure 1-2. Digital photographs of electrospun nanofiber mats of (a) as-prepared PAN, (b) CNF after stabilization, (c) CNF/ACNF after calcination, and (d) the CNF/ACNF nanoparticles after manual grinding using pestle and mortar.

2. Preparation of ACNF@PCL and ACNF-PCL nanofiber mats

I prepared two different ACNF NPs-containing PCL nanofiber mat groups, viz. ACNF@PCL and ACNF-PCL. Firstly, PCL electrospun nanofiber mat was prepared from

the 7 mL of 10% (w/v) PCL solution in HFIP medium following the experimental parameters, 0.7 mL/h flow rate, 15 kV voltage, and 1000-rpm rotor speed.

To prepare ACNF@PCL nanofiber mats, I cut the PCL mats into 8-mm circular disks using a hole-piercing tool. The disk-shaped mats were placed in three sets of 10-mL glass vials and wetted using EtOH. A 2 mL of ACNF NPs solution prepared at different concentrations (EtOH, 1, 3, and 5 mg/ mL) was added to the vials and incubated for 12 h to take place self-deposition of the nanoparticles over the mats (Figure 1-3).

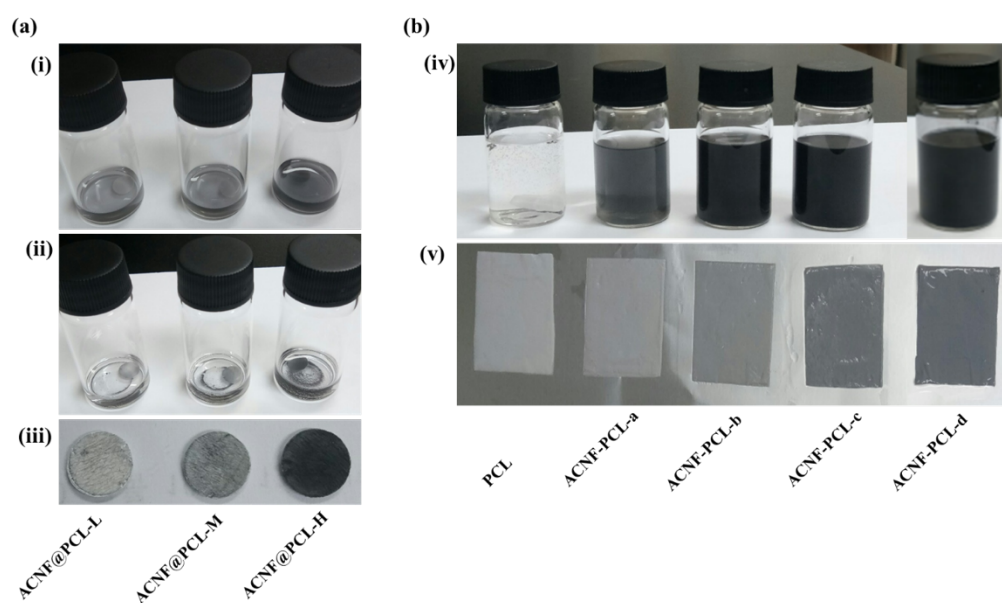


Figure 1-3. (a) Preparation of ACNF@PCL nanofiber mats. Incubation of ACNF NPs with the disc shaped mats at (i) 0 h, (ii) 12 h, and (iii) after drying in open air. (B) Preparation of PCL and ACNF-PCL nanofiber mats. (iv) The polymeric composite solution of PCL, ACNF-PCL-a, ACNF-PCL-b, ACNF-PCL-c, and ACNF-PCL-d, and (v) their electrospun nanofiber mats (wet by EtOH)

The resulting ACNF@PCL mats were washed with EtOH and agitated against water in a shaker, maintaining 120 rpm for 2 h to remove the non-adhered NPs from the mats. The

obtained mats were dried in the open air and labeled as ACNF@PCL-L, ACNF@PCL-M, and ACNF@PCL-H, respectively, for further characterizations. I determined the average concentration of NPs deposited on each mat by subtracting the weight of uncoated PCL mats from the weight of ACNF@PCL mats, which was 150–200 μg (ACNF@PCL-L), 300–400 μg (ACNF@PCL-M), and 700–800 μg (ACNF@PCL-H).

The ACNF-PCL nanofiber mats were prepared by electrospinning the polymeric composites of PCL (7 mL, 10 wt.%) and ACNF NPs (0.1, 0.4, 1.6, and 3.2 mg/mL). The experimental parameters were the same as specified for the preparation of the PCL nanofiber mat. The obtained mats were labeled as ACNF-PCL-a, ACNF-PCL-b, ACNF-PCL-c, and ACNF-PCL-d, respectively. The digital images of polymeric composites of PCL and ACNF NPs, and the EtOH wetted nanofiber mats have been shown in Figure 1-3.

3. Bradford assay

Bradford assay, alternatively known as bicinchoninic acid assay (BCA), was performed to quantify protein adsorption onto the nanoparticles colorimetrically using the Abbkine protein quantification kit. A calculated concentration range of nanoparticles (50–2500 $\mu\text{g}/\text{mL}$) was dispersed in 200 $\mu\text{g}/\text{mL}$ concentrated BSA solution in PBS at 25°C. After incubation for 2h, the solution was centrifuged at 3000rpm to separate the protein adsorbed nanoparticles from the free protein solution in the supernatant. The particles were washed three times with distilled water and then redispersed in 150 μL of PBS. An equal amount of Bradford reagent (2 \times) was added to the solution. After incubation for 2 h at 37 °C, the absorbance of the solution was recorded at 562 nm using an Infinite F50 microplate reader (TECAN, Switzerland). Previously, BSA solution at different concentrations (0.5–100 $\mu\text{g}/\text{mL}$) was subjected to the assay to determine the slope value from the standard linear plot of protein concentration vs. absorption.

4. In vitro cell culture experiments

The CNF and ACNF nanoparticles were dispersed in PBS buffer to prepare a stock solution of 500 $\mu\text{g}/\text{mL}$, which was sterilized under UV light for 12 h before the in vitro cell-related experiments. NIH3T3 mouse embryonic fibroblast cell line was procured from Sigma Aldrich, and the cultivation of cells was processed in a DMEM medium (Gibco, US) containing 10% fetal bovine serum and 1% penicillin in an incubator maintaining a 5% of CO₂ atmosphere at 37 °C. A 500 μL of NIH3T3 cells (5×10^4 cell density) were seeded into a 48-well tissue culture plate. After 12 h of cell culture, experimental nanoparticles (5–100 $\mu\text{g}/\text{mL}$) were added to the plate with uttermost care without disturbing the adhered cells. The nanoparticle-treated cells were investigated using different cell-related studies such as cell counting kit-8 (CCK-8), lactate dehydrogenase (LDH), and live and dead cell assays on different incubational periods at 24 h and 48 h.

The culture medium was replaced for the CCK assay by a 500 μL of CCK reagent (Boya Biotech, China) solution in DMEM (1:9, v/v). After incubation for 1.5 h, 100 μL of the supernatant was transferred to a 96-well plate to measure the absorbance at 450 nm using the microplate reader. In the case of LDH assay, 100 μL of the supernatant was collected and mixed with the same volume of LDH reagent solution containing catalyst (diaphorase/NAD⁺) and dye (iodotetrazolium chloride and sodium lactate) in a 96-well plate. After 1 h of incubation, the absorbance of the solution was measured at 490 nm using the microplate reader.

The control was the cells without the treatment of nanoparticles, and the blank was the reagent solution for both assays. The cells were stained with the combined dye solution of 2 μM calcein AM and 4 μM ethidium homodimer-1 in PBS (LIVE/DEAD® Viability/Cytotoxicity Assay Kit). After 30 min of incubation at 25 °C, the images were obtained using the optical microscope equipped with a fluorescence light source and filters.

A wound scratch assay was performed when the cells reached 90% of confluency. A scratch was made using a 100- μ L pipette tip, and subsequently, 20 μ g/mL of concentrated nanoparticles were added. The wound area was monitored for different periods 4, 8, 12, and 24 h using the optical microscope, and the remaining wound area was measured using ImageJ software.

5. Cell proliferation study

While analyzing the cell proliferation of NIH3T3 cells (5×10^4 cell density) on PCL, ACNF@PCL, and ACNF-PCL nanofiber mats by CCK, the measurement was carried out at different incubational periods (1, 3, and 5 days). The mats were sterilized under UV light for 12 h prior to the measurement.

For the observation of CLSM images, the specimen was prepared as follows: fixation in buffered formalin (15 min), permeabilization with 0.5% Triton X-100 (10 min), and subsequently blocked with 2.5% bovine serum albumin (10 min). The cells were stained by the incubation of 500 μ L of dye mixture containing Alexa Fluor®594 phalloidin and DAPI for 20 min.

For SEM analyses of the samples, the samples were fixed in buffered formalin (15 min) and subsequently incubated with increasing concentrations of EtOH in water (50, 80, and 100%). Then, the samples were air-dried for 12 h before the measurement.

6. Statistical analysis

All the experimental data were expressed as mean \pm standard deviation from the results of at least three independent measurements. One-way ANOVA with a post-hoc Tukey test

was performed to determine the statistical differences between different groups. The level of statistical significance was described as * $p < 0.05$ and ** $p < 0.01$.

III. Results and Discussion

1. Physicochemical properties and cytotoxicity of CNF and ACNF NPs

SEM observation and spectral characterizations (FTIR, XPS, and Raman) were carried out to confirm the transformation of PAN into CNF and ACNF. As shown in Figure 2-1a, SEM images revealed that all PAN, CNF, and ACNF nanofibers were cylindrically shaped, but ACNF nanofibers alone exhibited roughness on their surface.

The nanofibers in the ACNF mat have shrunken together by combining alkali treatment and calcination processes. The fiber diameter range of CNF and ACNF nanofibers has been almost equal with 312 ± 68 nm and 280 ± 100 nm, respectively, whereas PAN nanofibers have a larger diameter (558 ± 93 nm) (Figure 2-1b). I found that the size of the ACNF NPs (565–3322 nm) was smaller than CNF NPs (682–4129 nm) about their length after grinding, which indicates that the ACNF fiber mat was more brittle and susceptible to being broken down (Figure 2-1c).

FTIR spectra were performed to analyze the functional groups present in the samples (Figure 2-2). PAN showed its characteristic $-C \equiv N$ vibrational band at 2243 cm^{-1} and C-H vibrational bands of aliphatic -CH and -CH₂ groups at different regions such as 2933, 1448, 1362, 1241, and 1073 cm^{-1} . The C-C stretching vibrational mode has been observed at 1631 cm^{-1} . PAN undergoes several molecular transformations during stabilization and carbonization. The aliphatic chain adopts the aromatic structure by evaporating heteroatomic gases like N₂, H₂O, H₂, NH₃, and HCN²⁸.

The FTIR trace of CNF is evident with the disappearance of the nitrile peak (2243 cm^{-1}). There was a significant reduction in the intensity of the C-H stretching vibrational bands reflected at 2933 , 1448 , and 1362 cm^{-1} . Furthermore, CNF demonstrated two typical broad peaks centered around 1627 and 1113 cm^{-1} . The former peak represents a combination of C=N, C-N, and C=C vibrational bands, and the latter indicates the traces of O-H, C-O-C, and N-H vibrational bands.

In the case of ACNF's FTIR spectrum, the peaks are almost similar to CNF. However, the peaks are widened comparatively, suggesting that ACNF has incorporated more hydroxyl and carbonyl groups by the treatment of KOH during the carbonization process²⁷. These results were consistent with the previous literature reports^{29,30}.

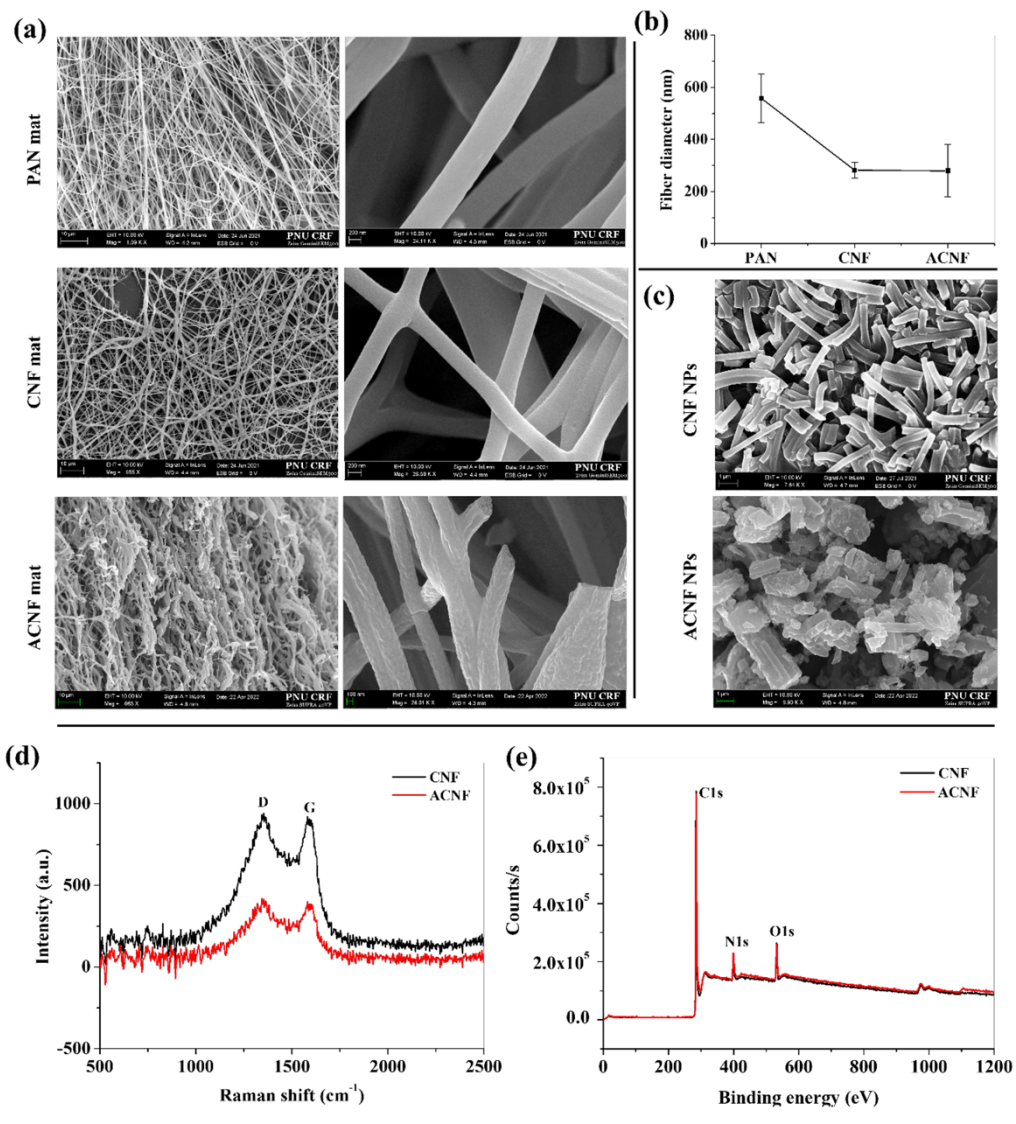


Figure 2-1. **a** SEM images of electrospun PAN, CNF, and ACNF nanofiber mats at different scale bar 10 μm and 200 nm, and **b** their respective fiber diameter profile. **c** SEM images of CNF and ACNF nanoparticles obtained after grinding the mats (scale bar 1 μm). **d** Raman and **e** XPS spectra of CNF and ACNF NPs

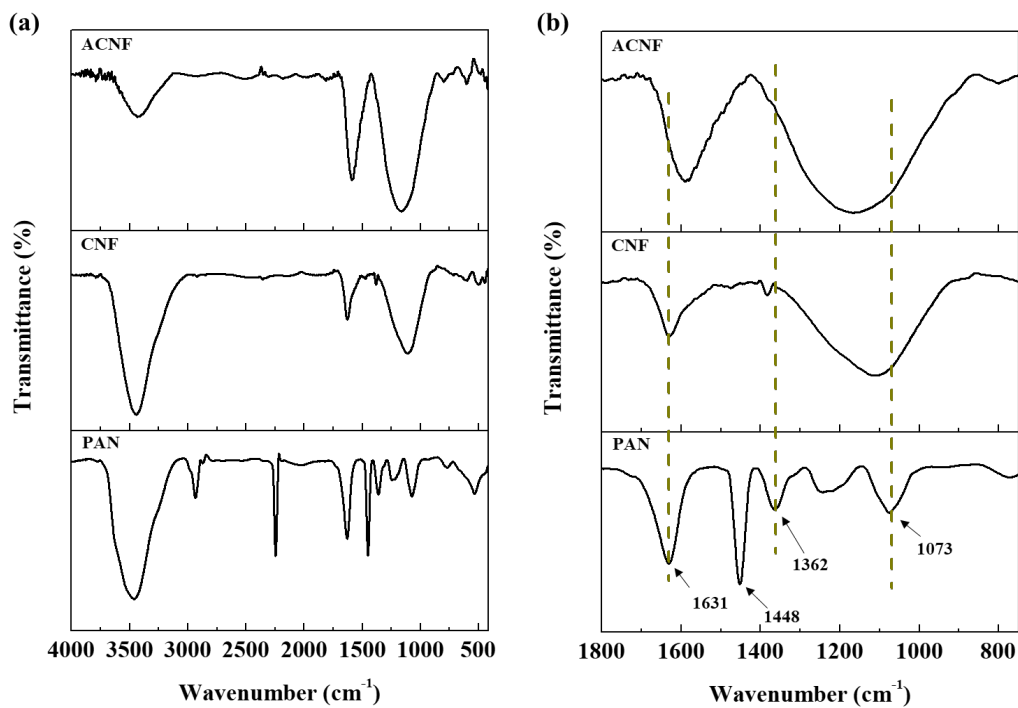


Figure 2-2. (a) FTIR spectra of PAN, CNF, and ACNF NPs. (b) The wavenumber range (800 - 1800 cm⁻¹) has been shown in expanded form. The dashed line indicates the shift in wavenumber.

Raman spectra of CNF and ACNF were helpful in providing structural information like the degree of graphitization and disorderness (Figure 2-1d). The disordered carbon (D) and graphitic carbon peaks (G) were identified at 1348 cm⁻¹ and 1590 cm⁻¹, respectively. The ID/IG ratio, a measure of D-band intensity relative to the G-band, represents the graphitization degree³¹. The samples CNF and ACNF had the ID/IG ratio of 1.03 and 1.05, respectively, indicating that ACNF has exhibited a slightly lower graphitization extent than CNF.

X-ray photoelectron spectroscopy (XPS) determined the elemental composition of the carbonaceous materials. As shown in Figure 2-1e, the wide survey XPS spectra of CNF and ACNF have displayed three different peaks to indicate the presence of carbon (290.8 eV), nitrogen (405.3 eV), and oxygen (537.0 eV). The Raman and XPS spectra were in close agreement with the previous reports^{31,32}.

The cell culture medium contains adhesive proteins and growth factors for the growth and multiplication of the cells. It is a fact that the NPs can interact with the cells indirectly through protein coronas³³. Hence, I studied protein adsorption onto the nanoparticles quantitatively using the colorimetric Bradford assay. As shown in Figure 2-3, the results revealed that the quantity of adsorbed protein on ACNF NPs was higher than that of CNF NPs at all the concentration range ($p < 0.001$). Mainly, ACNF NPs, at 2500 $\mu\text{g/mL}$ concentration, have adsorbed 149 μg of protein with a two-fold increase compared to CNF NPs (74 μg). It is inferred that the larger surface area of ACNF NPs has influenced to have more protein adsorption.

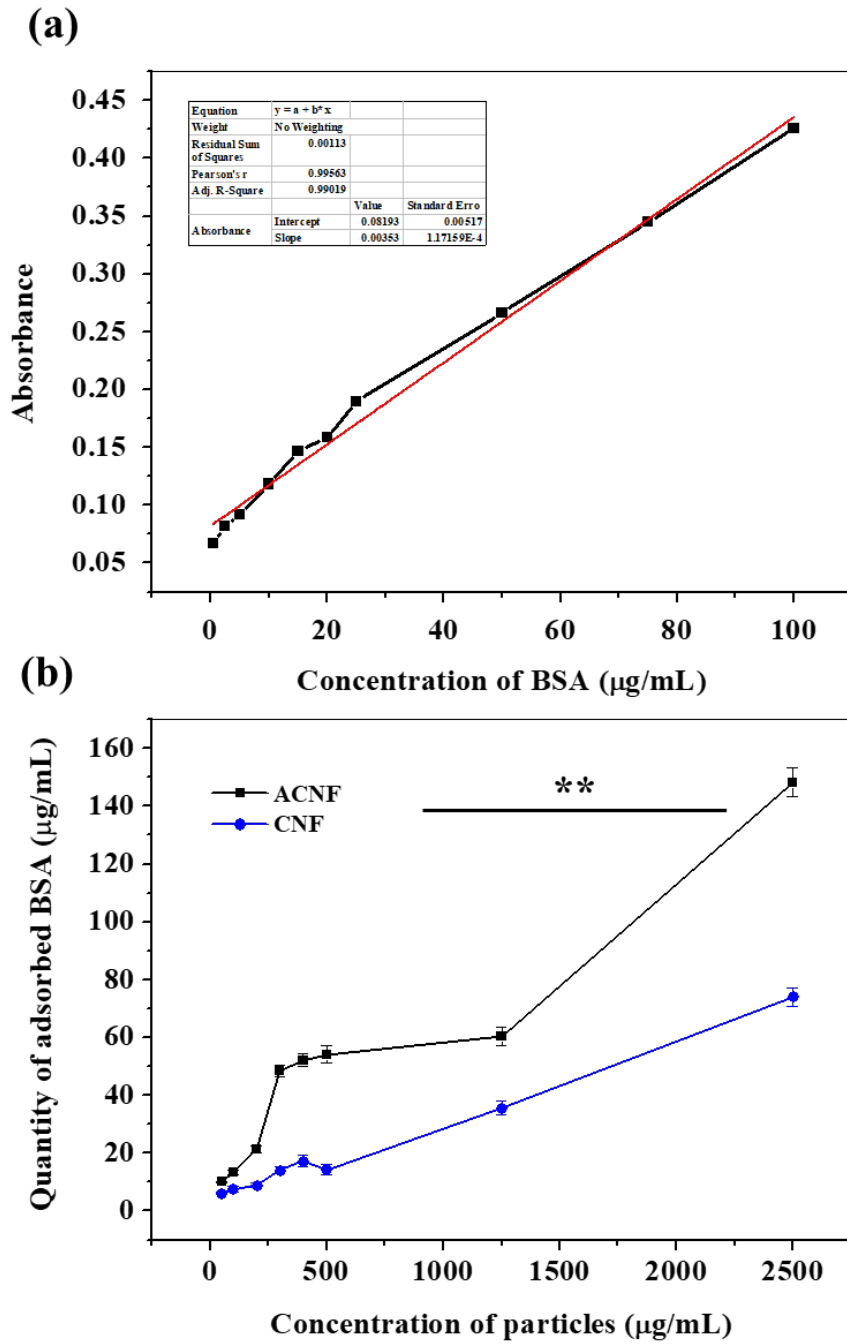


Figure 2-3. (a) A linear plot curve between the concentration of standard BSA solution and

their optical absorption at 562 nm. (b) A comparison of protein adsorption between various concentrated CNF and ACNF NPs (0.5 - 100 $\mu\text{g}/\text{mL}$). Statistical value $p < 0.001$.

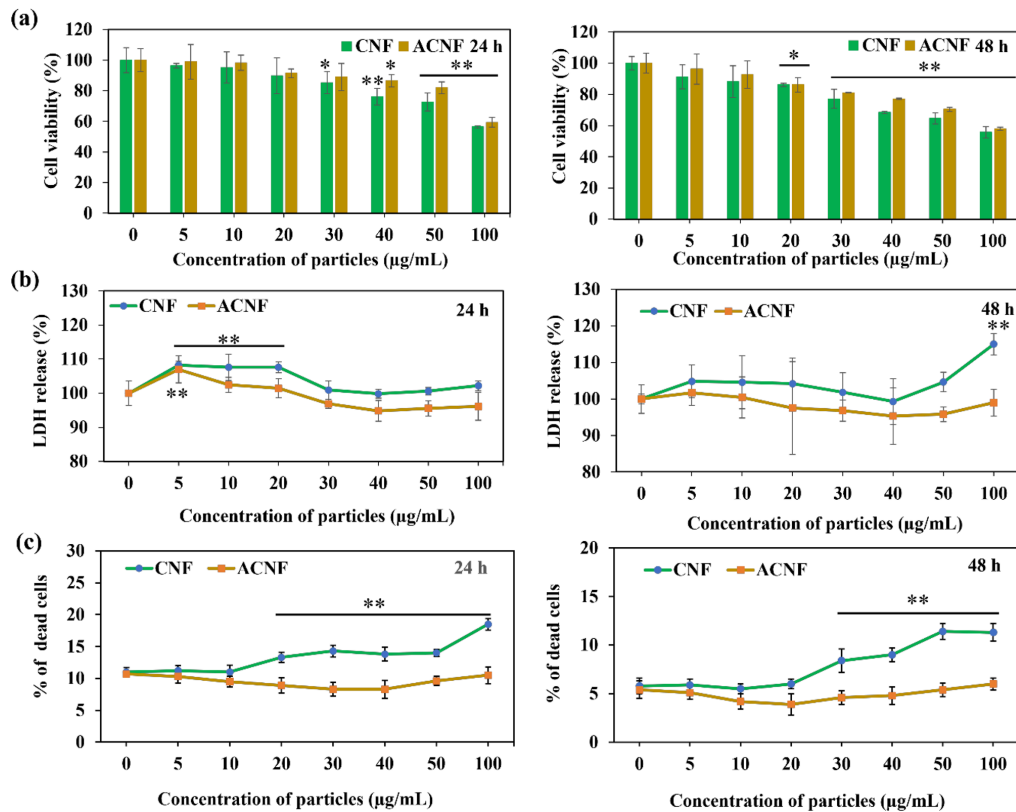


Figure 3-1. In vitro cell line studies of CNF and ACNF NPs using NIH3T3 fibroblasts by the **a** percentage of cell viability, **b** LDH release, and **c** dead cells on different periods of 24 h and 48 h

Cell biocompatibility of CNF and ACNF nanoparticles (5–100 $\mu\text{g}/\text{mL}$) was examined at 24 h and 48 h, using CCK, LDH, and live and dead cell assays, as shown in Figure 3-1 a–c. CCK assay showed a dose-dependent decrease in cell viability for both CNF and ACNF NPs. The sample ACNF has accounted for more cell viability (%) than CNF at each concentration of the nanoparticles. There was no significant difference compared to control

in their cell viability up to the concentration of 20 $\mu\text{g/mL}$ at 24 h and 10 $\mu\text{g/mL}$ at 48 h. However, I could observe a significant difference ($p < 0.001$) for both nanoparticles at $\geq 30 \mu\text{g/mL}$ concentrations at 48 h of the study. The optical images of cells captured just before the measurement of the CCK assay have been shown in Figure 3-2.

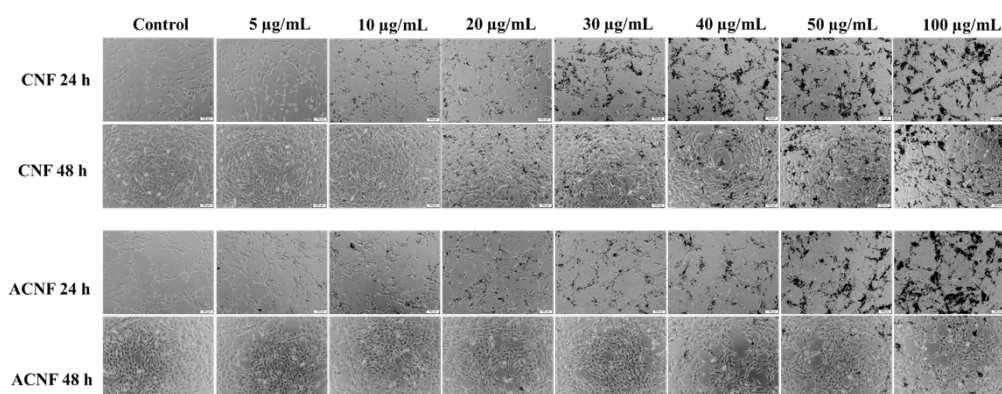


Figure 3-2. Optical microscope images of CNF or ACNF NPs (5 - 100 $\mu\text{g/mL}$) treated NIH3T3 cells at 24 and 48 h of incubational periods. Control is the untreated cells. The scale bar is 100 μm .

LDH assay monitors cell membrane integrity by quantifying the released lactate dehydrogenase into the medium, corresponding to the number of damaged cells³⁴. According to LDH release, 5–20 $\mu\text{g/mL}$ concentrated CNF NPs showed toxicity with a significant difference of $p < 0.001$ at 24 h, whereas ACNF NPs displayed the same level of toxicity at 5 $\mu\text{g/mL}$ concentration only. At 48 h of the study, only CNF NPs (100 $\mu\text{g/mL}$) showed a significant difference at $p < 0.001$. In addition, I demonstrated cell viability by counting the live/dead cells after staining the nucleus and cytoplasm, and fluorescent images of the same have been shown in Figure 3-3, the results of which were found to reflect the outcome of the LDH release pattern. CNF NPs demonstrated a high percentage of dead cells compared to ACNF NPs and showed a significant difference compared to control at and above 20 $\mu\text{g/mL}$ (24 h) and 30 $\mu\text{g/mL}$ (48 h) of the NP concentration.

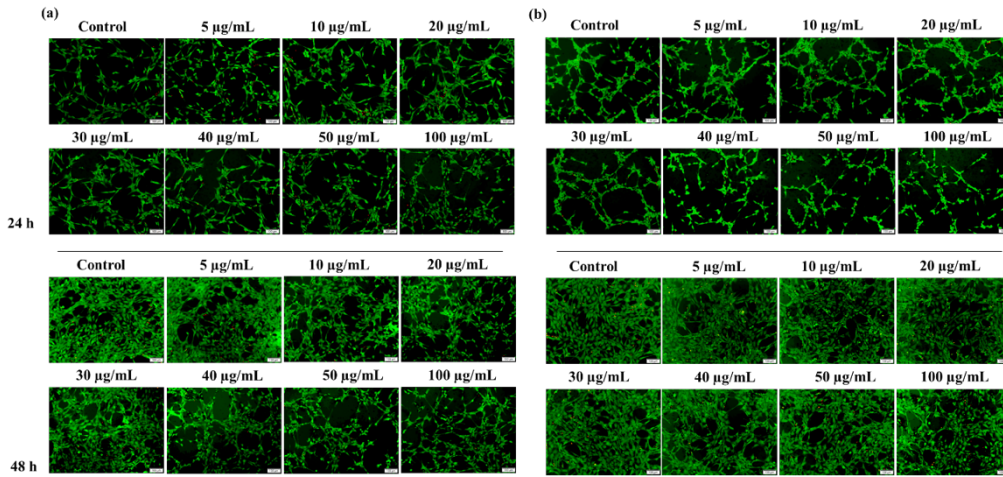


Figure 3-3. Fluorescent microscope images of live and dead cells after treatment with (a) CNF or (b) ACNF NPs (5 - 100 μg/mL) on different incubational periods, 24 and 48 h. The control is the cell line without treatment. Scale bar is 100 μm.

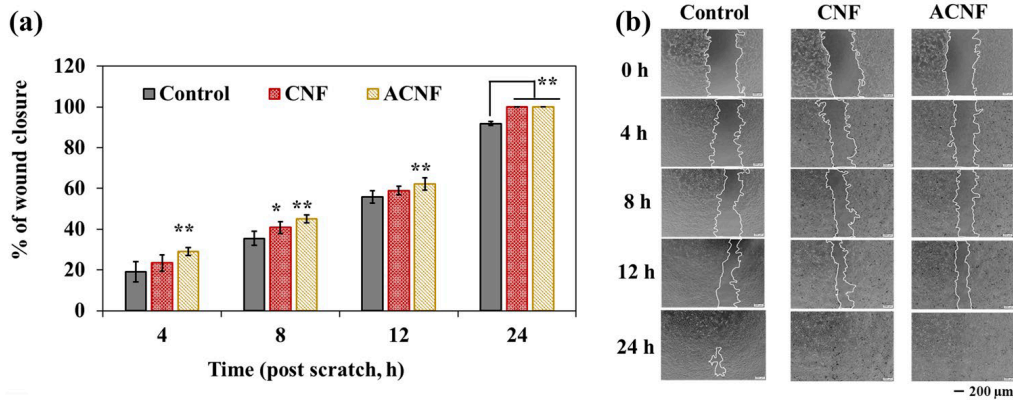


Figure 4-1. In vitro wound scratch assay using NIH3T3 fibroblasts. **a** The percentage of wound closure for control (untreated), CNF, and ACNF NPs were estimated at 4, 8, 12, and 24 h of post-wound creation. **b** Optical images of the cells have been shown with a scale

bar of 200 μm

I carried out an in vitro wound scratch assay to evaluate the wound healing potential of CNF and ACNF NPs. I selected 20 $\mu\text{g/mL}$ concentrated nanoparticles for evaluation as the cell biocompatibility profiles demonstrated the onset of toxicity above that concentration. As shown in Figure 4-1 and Figure 4-2, the percentage of wound closure was estimated for a 24-h duration after the scratched monolayer of the cells was treated with NPs. At the end of the study, I found that CNF and ACNF NPs healed the wound by 100% with the migration of cells to the damaged area, but the control still had the remaining wound area of about 8.2%. Meanwhile, ACNF NPs have slightly surpassed CNF NPs in the percentage of wound closure, showing a significant difference compared to untreated control ($p < 0.001$) at the investigation periods of 4, 8, and 12 h. The results demonstrate that both carbon fiber nanomaterials have the potential to act as chemoattractants helping for cell migration, the same of which has been observed for CNTs also by the researchers⁴.

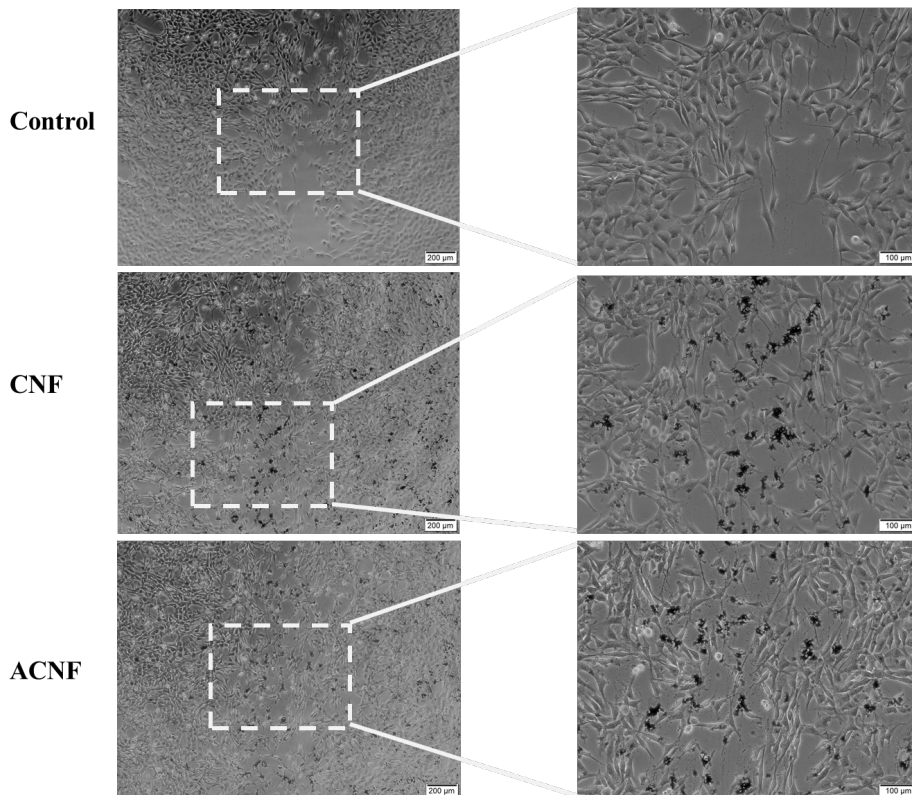


Figure 4-2. An enlarged view of the optical microscope images of the NPs treated cells after 24 h in in vitro wound healing.

Overall, the physicochemical and cell line-related characterizations of CNF and ACNF NPs demonstrate that ACNF NPs is a better candidate than CNF NPs in terms of size, protein adsorption, cell compatibility, and in vitro wound healing potential. Hence, I processed ACNF NPs to prepare NP-containing nanofiber mats as the cell scaffolds for the subsequent cell proliferation studies.

2. Surface properties of ACNF@PCL and ACNF-PCL mats

According to the DLS measurement, the average hydrodynamic diameter, polydispersity

index, and zeta potential of the colloidal ACNF NPs were observed to be 1808 ± 37 d. nm, 0.546 ± 0.029 , and -22.4 ± 3.2 mV, respectively (Figure 5(a), (b)). I infer that the ACNF NPs have a large size with moderate distribution at a physiological pH of the solution. The negative sign of zeta potential is due to oxygen-containing functional groups on the NP surface. As the particles are larger and are not protected by the encapsulating agent, they aggregate and settle at the bottom after 24-h incubation. However, I observed that the dispersion of ACNF NPs in PCL polymeric solution in HFIP maintained the colloidal stability even after incubation because the polymeric moieties surrounded the NPs (Figure 5(c)).

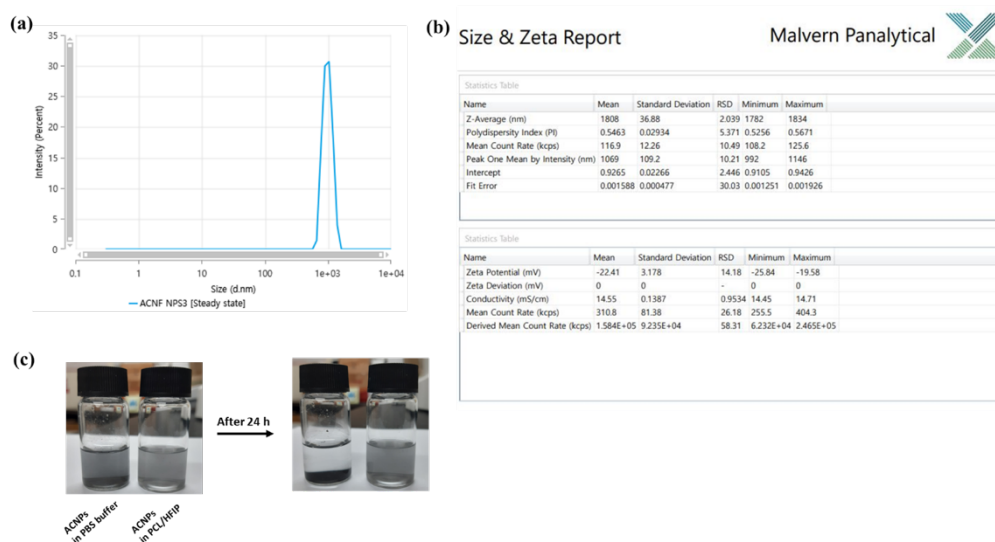


Figure 5. The hydrodynamic size and zeta potential reports (a, b) provide information about the colloidal stability of the ACNF NPs in PBS solution. (c) The digital images of ACNF NPs in PBS and PCL polymeric solution in HFIP medium after incubation for 24 h.

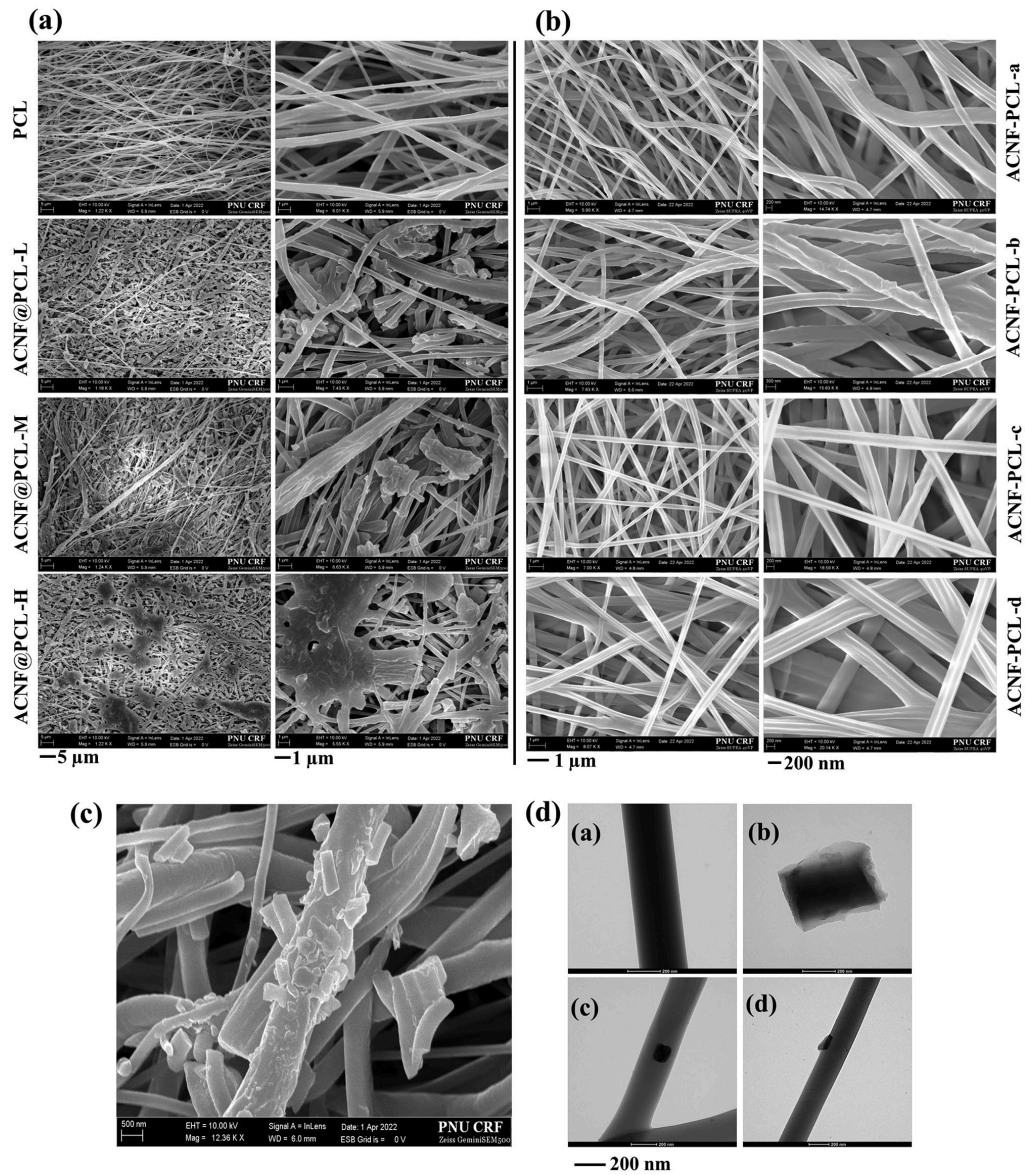


Figure 6. SEM images of ACNF@PCL **a** and ACNF-PCL **b** nanofiber mats at different magnifications (5 μm , 1 μm , and 200 nm). **c** SEM image of ACNF@PCL-L showing adhered nanoparticles over the single nanofiber (scale bar 500 nm). **d** TEM images of PCL single nanofiber (i), ACNF NPs (ii), and the presence of ACNF NPs in the core (iii) and edge parts (iv) of the ACNF-PCL-a mat's single nanofiber (scale bar 200 nm)

Hence, I expect that the NPs be found in the aggregated state in PBS solution or over ACNF@PCL scaffolds but in the dispersed state in the ACNF-PCL scaffolds during microscopic analyses. SEM images of ACNF@PCL and ACNF-PCL nanofiber mats were captured to observe the presence of ACNF NPs and changes in fiber morphology. As expected, the ACNF@PCL-H mat possessed many ACNF NPs compared to ACNF@PCL-L and ACNF@PCL-M mats (Figure 6a). A spread of individual NPs is present over ACNF@PCL-L and ACNF@PCL-M mats. In contrast, a densely packed structure of NPs can be seen over the ACNF@PCL-H mat due to the accumulation of more concentrated NPs by self-deposition. The NPs are not only entrapped into the fiber mesh of the mat, but they have also firmly adhered to each PCL nanofiber, which is evident from Figure 6c. As far as SEM images of ACNF-PCL nanofiber mats are concerned, the morphology of the nanofiber from PCL to ACNF-PCL-c, cylindrically shaped with a fiber diameter of 175–485 nm, was not significantly changed, but ACNF-PCL-d nanofibers appear with drumstick-like structure with the diameter range of 313–570 nm (Figure 6b). In addition, most of the fibers in ACNF-PCL-d have been found stuck together. The reason might be the polymeric composite with a large amount of ACNF NPs has affected the surface morphology during electrospinning as the carbon nanomaterials are generally electroactive

35.

When I analyzed the TEM image of ACNF-PCL-a nanofibers, I found that ACNF NPs are present in the nanofiber's core and edge parts (Figure 6d). Water contact angle (θ) analyses revealed that both ACNF@PCL and ACNF-PCL nanofiber mats had increased wettability surface while increasing the concentration of ACNF to PCL (Figure 7). The sample PCL exhibited more water contact angle value with $134.3 \pm 0.7^\circ$, whereas the ACNF@PCL-H mat has registered less contact angle ($67.7 \pm 1.6^\circ$). The samples ACNF@PCL-L and ACNF@PCL-M have possessed $122.6 \pm 0.9^\circ$ and $115.1 \pm 1.2^\circ$, respectively. The ACNF-PCL mat groups have exhibited a value between the range of 120–

130.6°. The NPs have contained reactive functional groups on the surface area, and hence, they have provided wettability to the fiber surface, increasing hydrophilicity. As ACNF@PCL mats have NPs on the surface to interact readily with water molecules, their hydrophilic nature is far higher than ACNF-PCL mats. Scientific reports reveal that most animal cells thrive well on a moderate hydrophilic surface with a θ range of 5–150° as the wettable nature of a biomaterial can control essential protein adsorption³⁶.

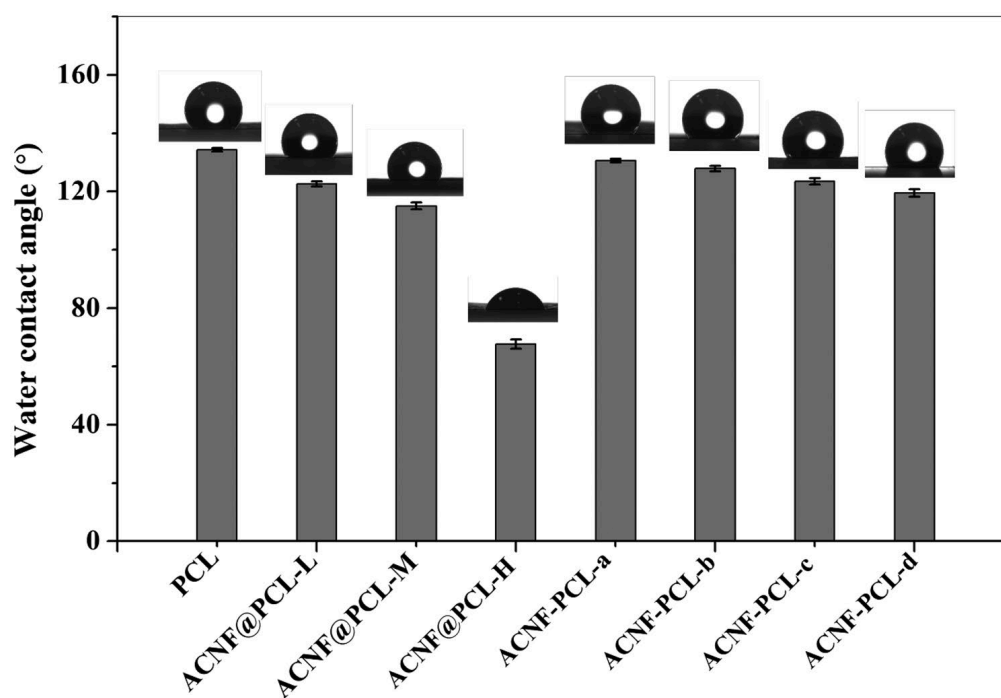


Figure 7. Water contact analysis revealing the wettability property of PCL, ACNF@PCL, and ACNF-PCL nanofiber mats

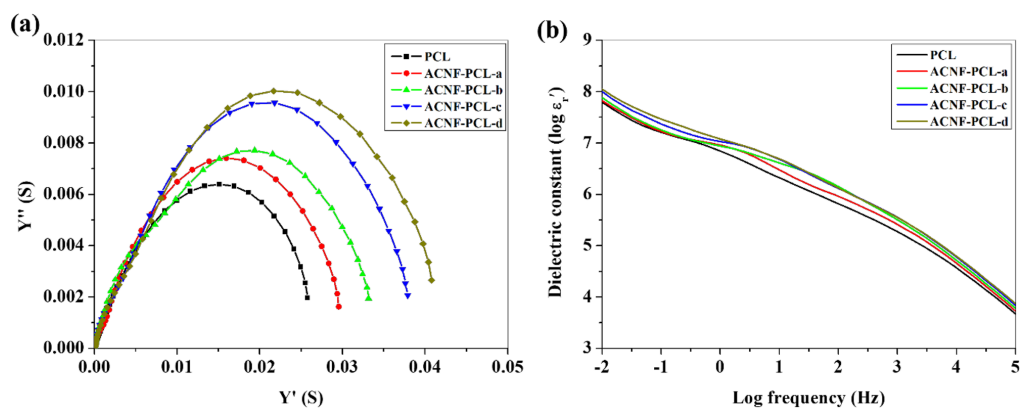


Figure 8. Electrochemical studies of PCL and ACNF-PCL mats showing a Nyquist admittance and b frequency-dependent dielectric constant curves. Y' , real part of admittance; Y'' , imaginary part of admittance; S, Siemens; ϵ' , real part of relative permittivity

I analyzed the AC impedance spectra of PCL and ACNF-PCL nanofiber mats to determine whether the incorporated ACNF NPs into the fiber have increased electrochemical properties. The Nyquist admittance plot (Figure 8a) shows that the entrapment of charged moieties by the fibers' functional groups has increased from PCL to ACNF-PCL-d, which is revealed by the steepness of curve ³⁷. From Figure 8b, I have determined the corresponding dielectric constant values of the mats at 0.01 Hz frequency as 7.79 ± 0.02 (PCL), 7.82 ± 0.03 (ACNF-PCL-a), 7.88 ± 0.03 (ACNF-PCL-b), 7.99 ± 0.02 (ACNF-PCL-c), 8.05 ± 0.03 (ACNF-PCL-d). It was reported that an increase in the dielectric constant value of a scaffold would favor cell proliferation ³⁸. In our previous research work, I demonstrated that increased dielectric constant by the addition of chitosan to PCL has contributed to improved cell proliferation on the scaffold ³⁹. I also recorded ATR-FTIR spectra of PCL and ACNF-PCL nanofiber mats to confirm the incorporation of NPs into PCL (Figure 2-4). PCL was confirmed by its characteristic peaks at 1728 cm^{-1} (C = O stretching), 1174 cm^{-1} (symmetric C–O–C stretching), 1239 cm^{-1} (asymmetric C–O–C stretching), and 1293 cm^{-1} (C–O and C–C stretching). None of the ACNF-PCL mats

(ACNF-PCL-a, ACNF-PCL-b, ACNF-PCL-c, and ACNF-PCL-d) showed either new peak formation or shift in wavenumber, which indicates that ACNF NPs are interacting with PCL by weak physical forces only. The characteristic peaks of NPs were also not observed in the spectra (studied in Figure 2-2) because the nanoparticles were incorporated into the nanofibers and were not freely available at the surface. The results were concordant with the previous research reports^{40, 41}.

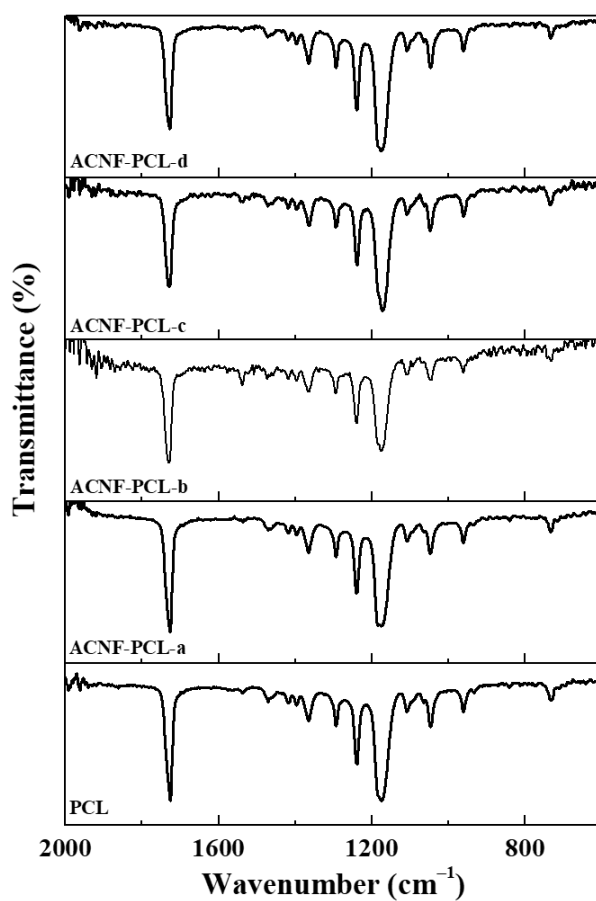


Figure 2-4. ATR-FTIR spectra of electrospun nanofiber mats of PCL and ACNF-PCL group. The wavenumber range of 600 - 2000 cm^{-1} has been shown.

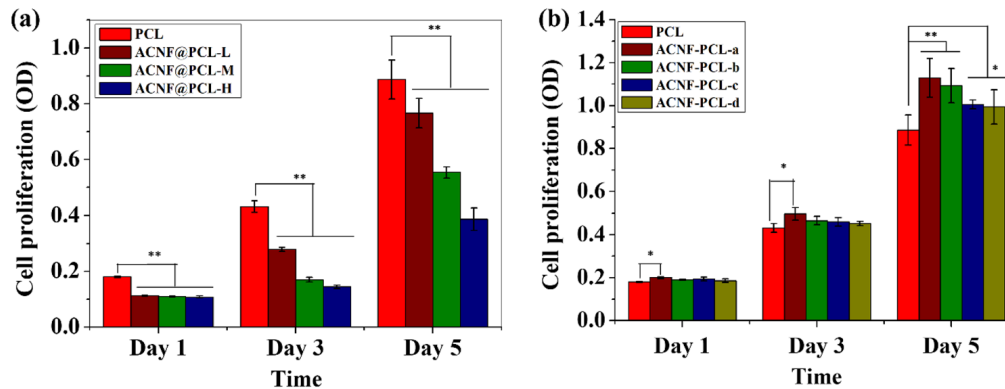


Figure 9. CCK assay demonstrating cell proliferation over PCL, **a** ACNF@PCL, and **b** ACNF-PCL scaffolds through optical density (OD) measurable at 450 nm on days 1, 3, and 5 of post-treatment. Inoculum cell density is 5×10^4 cells/well. $n = 5$; * $p < 0.05$, ** $p < 0.01$

3. Cell proliferation on ACNF@PCL and ACNF-PCL scaffolds

I analyzed cell proliferation on ACNF@PCL nanofiber mats to investigate cell biocompatibility when the cells are close to the adhered ACNF NPs on the mats. CCK assay demonstrated that the ACNF NPs deposited on PCL mats have not supported cell proliferation and triggered cell toxicity while increasing the NPs' concentration from ACNF@PCL-L to ACNF@PCL-H (Figure 9a). Hence, we observed cell proliferation profile in the following order, $PCL > ACNF@PCL-L > ACNF@PCL-M > ACNF@PCL-H$ on each day of cell proliferation with a significant difference ($p < 0.001$). In particular, the optical value registered for ACNF@PCL-H (0.38 ± 0.04) on day 5 was found to be less than that of PCL (0.43 ± 0.02) on day 3. Meanwhile, I have observed that NPs inside the fiber ACNF-PCL mat groups have promoted cell proliferation (Figure 9b). And the order of cell proliferation was also found as $ACNF-PCL-a > ACNF-PCL-b > ACNF-PCL-c > ACNF-PCL-d > PCL$. On the 5th day of cell proliferation, ACNF-PCL-a and ACNF-PCL-b mats showed a significant difference of $p < 0.001$ compared to PCL mat, while ACNF-

PCL-c and ACNF-PCL-d mats showed a difference at the level of $p < 0.05$. The CLSM images of cells grown on both mat groups on days 1, 3, and 5 have been shown in Figure 10, the results of which have been found to correspond to the CCK data. As ACNF@PCL-L and ACNF-PCL-a scaffolds have witnessed more cell proliferation than other scaffolds in their respective series, I captured their SEM images on days 1, 3, and 5. As shown in Figure 11-1 and Figure 11-2, it is apparently seen that cell morphology and cell-cell communication were not affected on any of the scaffolds by ACNF NPs.

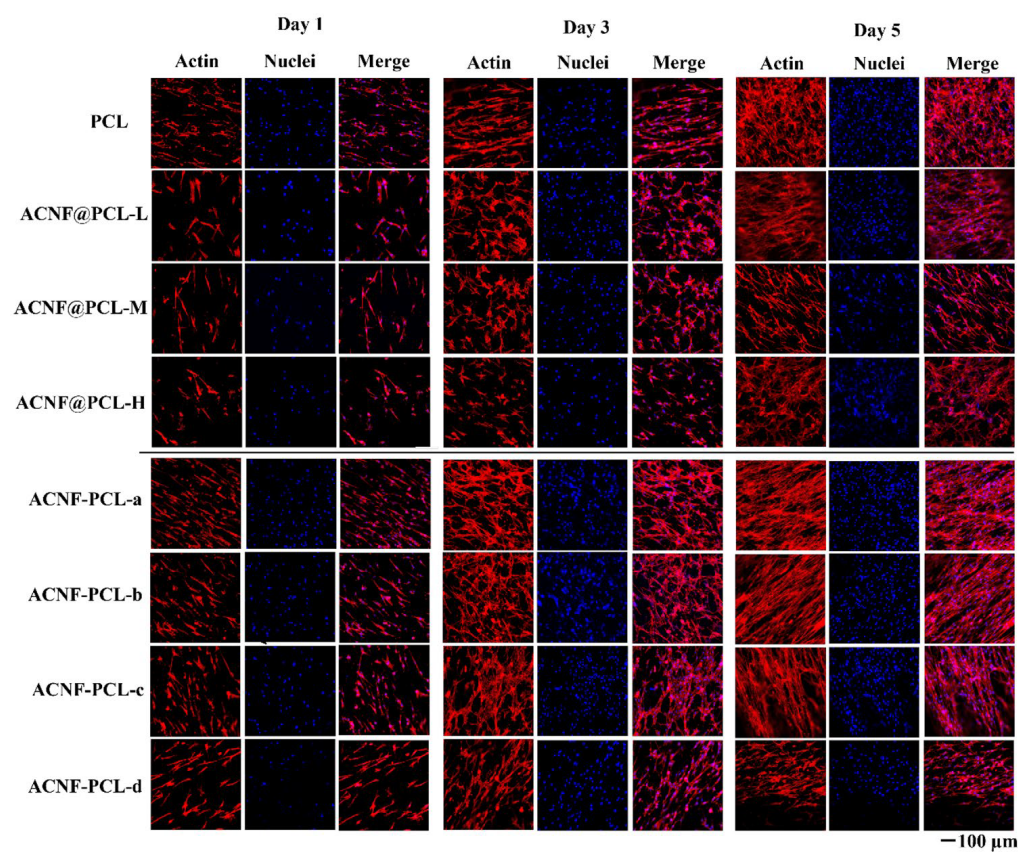


Figure 10. CLSM images of cell proliferation on PCL, ACNF@PCL, and ACNF-PCL scaffolds on days 1, 3, and 5 posttreatments with a scale bar of 100 μ m

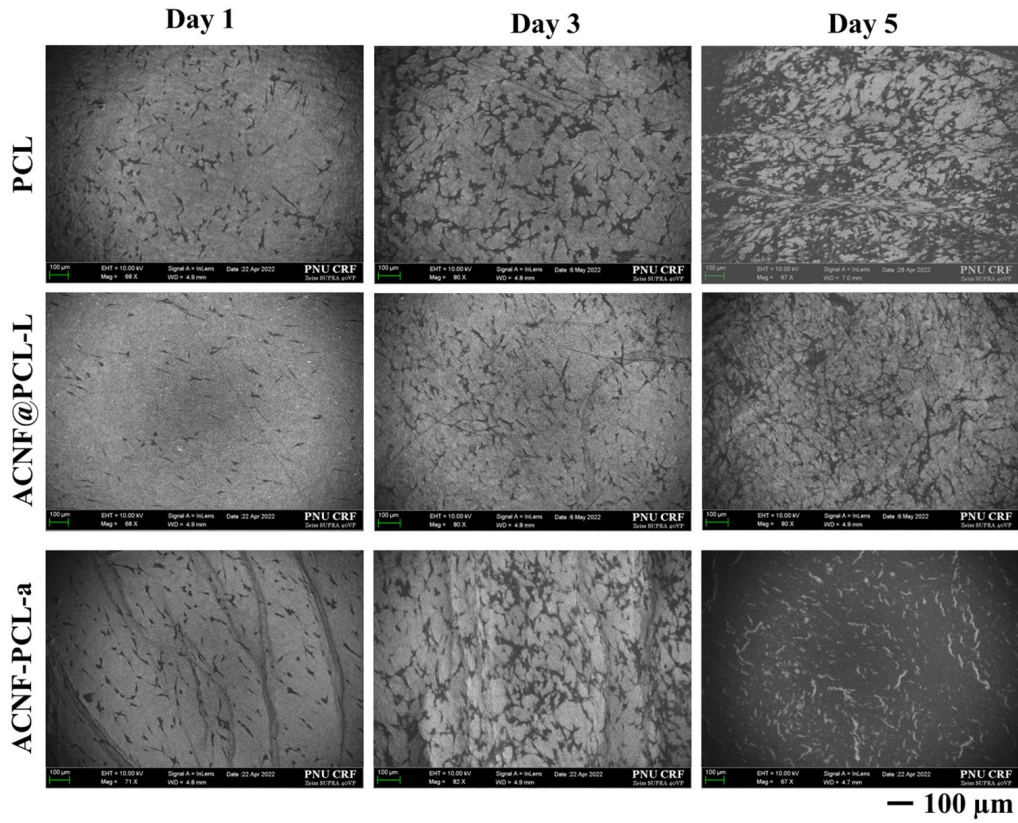


Figure 11-1. SEM images showing proliferated cells on PCL, ACNF@PCL-L, and ACNF-PCL-a nanofiber mats on days 1, 3, and 5 post-treatments (scale bar 100 μ m)

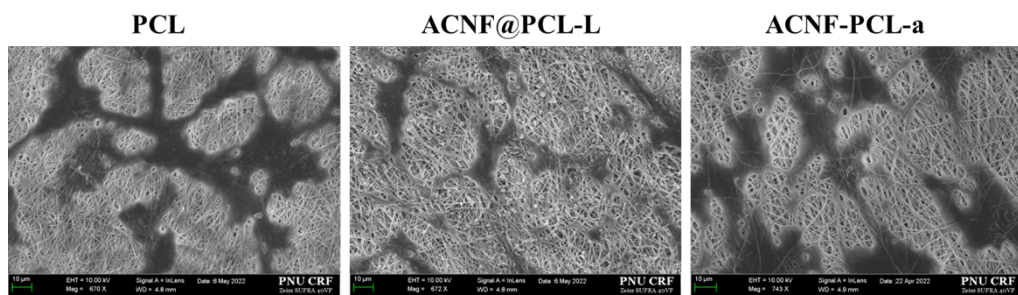


Figure 11-2. SEM images of cells grown on PCL, ACNF@PCL-L, and ACNF-PCL-a to demonstrate cell-cell communication on day 3. ACNF NPs can be clearly viewed in

ACNF@PCL-L scaffold.

There are some discussions on why ACNF NPs decreased cell proliferation gradually from ACNF-PCL-a to ACNF-PCL-b, though the ACNF-PCL mat group supported cell viability. The reason might be that wettability and dielectric properties are favorable factors in increased cell proliferation in ACNF-PCL mats compared to PCL. But, NP exposure was inevitable in ACNF-PCL fibers prepared by the conventional electrospinning method in the present work. I have already reported that the NPs are also present at the nanofiber's edge part, as evidenced by the TEM image (Figure 6d), which must be considered as they may have been involved in interaction with the cells to contribute to a bit of toxicity. Similar to our research work, More N. et al. prepared various graphene oxide (0.5, 1, 1.5, and 2%, w/v) nanoparticles reinforced poly(3-hydroxybutyrate-co-3-hydroxy valerate) piezoelectric electrospun nanofiber mats and found that GO incorporation into the scaffold promoted cell proliferation of freshly isolated goat chondrocytes at low concentration only (0.5%, w/v) on days 2, 5, and 7⁴².

Pan L. et al. fabricated different multiwall carbon nanotubes (MWNTs) / polycaprolactone composite scaffolds by the solvent evaporation technique with the addition of MWNTs (0.25, 0.5, 1, and 2 wt. %). They reported that the scaffold with a low concentration of 0.5 wt. % enhanced cell proliferation and differentiation of the rat bone-marrow-derived stromal cells (BMSCs) than that with high concentrations of MWNTs⁴³.

The systematic studies demonstrated that ACNF NPs are less biocompatible in free and bound states, but they can promote cell proliferation when incorporated into the nanofiber. By comparing cell compatibility among the investigated groups, the results were found ACNF-PCL-a > PCL > ACNF@PCL-L > ACNF NPs, and hence, I anticipate that the ACNF-PCL-a mat could be applied for skin tissue engineering. In our future work, I have planned to conduct a similar study by synthesizing smaller-sized NPs and preparing core-

shell nanofibers by coaxial electrospinning with NPs available only in the core part of the fiber to reflect a more significant difference in cell proliferation. Furthermore, I will resume in vivo animal studies using the optimized concentration of the NPs in the scaffolds to replicate the in vitro results. Besides, I will provide a deep insight into the ACNF's safety assessment by evaluating various toxicity profiles, such as genotoxicity and hemolytic activity.

IV Conclusion

In the present work, I have prepared ACNF NPs from the electrospun PAN nanofiber mat through synthetic procedures such as stabilization, alkali treatment, and calcination.

And, I developed ACNF NP-deposited mats (ACNF@PCL) and ACNF NP-incorporated mats (ACNF-PCL), varying the concentrations of NPs. I investigated their cell cytotoxicity and cell proliferation potential using NIH3T3 fibroblasts after evaluation of spectral and electron micrographs characterizations.

I observed that ACNF NPs cause a concentration-dependent cytotoxicity effect, which has been reflected in ACNF@PCL mat groups. Meanwhile, I noticed a progressive cell proliferation profile using ACNF-PCL mat groups. I found that ACNF-PCL-a promoted significant cell proliferation compared to PCL mat due to NPs' dielectric properties. I concluded that low concentrated ACNF NPs-incorporated PCL mat opts for skin tissue engineering.

References

1. Chen YC, Huang XC, Luo YL, Chang YC, Hsieh YZ, Hsu HY (2013) Non-metallic nanomaterials in cancer theranostics: a review of silica- and carbon-based drug delivery systems. *Sci Technol Adv Mater* 14:044407–044430

2. Georgakilas V, Perman JA, Tucek J, Zboril R (2015) Broad family of carbon nanoallotropes: classification, chemistry, and applications of fullerenes, carbon dots, nanotubes, graphene, nanodiamonds, and combined superstructures. *Chem Rev* 115:4744–4822
3. Wang W, Hou Y, Martinez D, Kurniawan D, Chiang WH, Bartolo P (2020) Carbon nanomaterials for electro-active structures: a review. *Polymers* 12: 2946
4. Ravanbakhsh H, Bao G, Mongeau L (2020) Carbon nanotubes promote cell migration in hydrogels. *Sci Rep* 10(1):2543
5. Zhang X, Li L, Ouyang J, Zhang L, Xue J, Zhang H, Tao W (2021) Electroactive electrospun nanofibers for tissue engineering. *Nano Today* 39:101196–101233
6. Lee SY, Jeon S, Kwon YW, Kwon M, Kang MS, Seong KY, Park TE, Yang SY, Han DW, Hong SW, Kim KS (2022) Combinatorial wound healing therapy using adhesive nanofibrous membrane equipped with wearable LED patches for photobiomodulation. *Sci Adv* 8:eabn1646–1660
7. Oriero DA, Weakley AT, Aston DE (2012) Rheological and micro-Raman time-series characterization of enzyme sol-gel solution toward morphological control of electrospun fibers. *Sci Technol Adv Mater* 13:025008–025018
8. Kang MS, Song SJ, Cha JH, Cho Y, Lee HU, Hyon SH, Lee JH, Han DW (2020) Increased neuritogenesis on ternary nanofiber matrices of PLCL and laminin decorated with black phosphorus. *J Ind Eng Chem* 92:226–235
9. Karuppanan KK, Panthalingal MK, Biji P (2018) Chapter 26 - Nanoscale, catalyst support materials for proton-exchange membrane fuel cells. In: C. Mustansar Hussain (Ed.), *Handbook of nanomaterials for industrial applications*. Elsevier (Amsterdam, Netherlands), pp. 468–495
10. Kim JG, Kim HC, Kim ND, Khil MS (2020) N-doped hierarchical porous hollow carbon nanofibers based on PAN/PVP@SAN structure for high performance supercapacitor. *Compos B Eng* 186:107825–107833

11. Guadagno L, Raimondo M, Vittoria V, Vertuccio L, Lafdi K, De Vivo B, Lamberti P, Spinelli G, Tucci V (2013) The role of carbon nanofiber defects on the electrical and mechanical properties of CNF-based resins. *Nanotechnology* 24:305704
12. Gao P, Li AR, Tai MH, Liu ZY, Sun DD (2014) A hierarchical nanostructured carbon nanofiber-In₂S₃ photocatalyst with high photodegradation and disinfection abilities under visible light. *Chem Asian J* 9:1663–1670
13. Marangon I, M.nard-Moyon C, Silva AKA, Bianco A, Luciani N, Gazeau F (2016) Synergic mechanisms of photothermal and photodynamic therapies mediated by photosensitizer/carbon nanotube complexes. *Carbon* 97:110–123
14. Wang Y, Qiu M, Won M, Jung E, Fan T, Xie N, Chi S-G, Zhang H, Kim JS (2019) Emerging 2D material-based nanocarrier for cancer therapy beyond graphene. *Coord Chem Rev* 400:213041
15. Selvaraj AR, Raja IS, Chinnadurai D, Rajendiran R, Cho I, Han DW, Prabakar K (2022) Electrospun one dimensional (1D) pseudocapacitive nanorods embedded carbon nanofiber as positrode and graphene wrapped carbon nanofiber as negatrode for enhanced electrochemical energy storage. *J Energy Storage* 46:103731–103731
16. Yadav D, Amini F, Ehrmann A (2020) Recent advances in carbon nanofibers and their applications - a review. *Eur Polym J* 138:109963–109976
17. Raja IS, Preeth DR, Vedhanayagam M, Hyon SH, Lim D, Kim B, Rajalakshmi S, Han DW (2021) Polyphenols-loaded electrospun nanofibers in bone tissue engineering and regeneration. *Biomater Res* 25:1–16
18. Farzamfar S, Salehi M, Tavangar SM, Verdi J, Mansouri K, Ai A, Malekshahi ZV, Ai J (2019) A novel polycaprolactone/carbon nanofiber composite as a conductive neural guidance channel: an in vitro and in vivo study. *Prog Biomater* 8:239–248

19. Mirzaei E, Ai J, Ebrahimi-Barough S, Verdi J, Ghanbari H, Faridi-Majidi R (2016) The differentiation of human endometrial stem cells into neuron-like cells on electrospun PAN-derived carbon nanofibers with random and aligned topographies. *Mol Neurobiol* 53:4798–4808
20. Shin YC, Yang WJ, Lee JH, Oh JW, Kim TW, Park JC, Hyon SH, Han DW (2014) PLGA nanofiber membranes loaded with epigallocatechin-3-O-gallate are beneficial to prevention of postsurgical adhesions. *Int J Nanomed* 9:4067–4078
21. Arampatzis AS, Kontogiannopoulos KN, Theodoridis K, Aggelidou E, Rat A, Willems A, Tsvintzelis I, Papageorgiou VP, Kritis A, Assimopoulou AN (2021) Electrospun wound dressings containing bioactive natural products: physico-chemical characterization and biological assessment. *Biomater Res* 25:1–21
22. Alven S, Buyana B, Feketshane Z, Aderibigbe BA (2021) Electrospun nanofibers/nanofibrous scaffolds loaded with silver nanoparticles as effective antibacterial wound dressing materials. *Pharmaceutics* 13:964–981
23. Ahire JJ, Hattingh M, Neveling DP, Dicks LM (2016) Coppercontaining anti-biofilm nanofiber scaffolds as a wound dressing material. *PLoS ONE* 11:e0152755–e0152766
24. Rather HA, Thakore R, Singh R, Jhala D, Singh S, Vasita R (2018) Antioxidative study of cerium oxide nanoparticle functionalized PCL-gelatin electrospun fibers for wound healing application. *Bioact Mater* 3:201–211
25. Lee JY, Kang TH, Choi JH, Choi IS, Yu WR (2018) Improved electrical conductivity of poly(ethylene oxide) nanofibers using multi-walled carbon nanotubes. *AIP Adv* 8:035024–035034
26. Bateni F, Hashemi Motlagh G (2022) Electrospun polyamide/graphene oxide nanofibers as fillers for polyethylene: preparation and characterization. *J Appl Polym Sci* 139:51506–51520

27. Yoon SH, Lim S, Song Y, Ota Y, Qiao W, Tanaka A, Mochida I (2004) KOH activation of carbon nanofibers. *Carbon* 42:1723–1729
28. Xu W, Xin B, Yang X (2020) Carbonization of electrospun polyacrylonitrile (PAN)/cellulose nanofibril (CNF) hybrid membranes and its mechanism. *Cellulose* 27:3789–3804
29. Mogolodi Dimpe K, Nomngongo PN (2019) Application of activated carbon-decorated polyacrylonitrile nanofibers as an adsorbent in dispersive solid-phase extraction of fluoroquinolones from wastewater. *J Pharm Anal* 9:117–126
30. Kamran U, Choi J, Park SJ (2020) A role of activators for efficient CO₂ affinity on polyacrylonitrile-based porous carbon materials. *Front Chem* 8:710–710
31. Chen Y, Liu Q, Wang J (2016) Carbon dioxide activated carbon nanofibers with hierarchical micro-/mesoporosity towards electrocatalytic oxygen reduction. *J Mater Chem A* 4:5553–5560
32. Zhang Z, Deng X, Sunarso J, Cai R, Chu S, Miao J, Zhou W, Shao Z (2017) Two-step fabrication of Li₄Ti₅O₁₂-coated carbon nanofibers as a flexible film electrode for high-power lithium-ion batteries. *ChemElectroChem* 4:2286–2292
33. Khan S, Gupta A, Verma NC, Nandi CK (2015) Kinetics of protein adsorption on gold nanoparticle with variable protein structure and nanoparticle size. *J Chem Phys* 143:164709–164718
34. Song SJ, Raja IS, Lee YB, Kang MS, Seo HJ, Lee HU, Han DW (2019) Comparison of cytotoxicity of black phosphorus nanosheets in different types of fibroblasts. *Biomater Res* 23:1–7
35. Zhang Z, Klausen LH, Chen M, Dong M (2018) Electroactive scaffolds for neurogenesis and myogenesis: graphene-based nanomaterials. *Small* 14:e1801983–e1802004
36. Chen L, Yan C, Zheng Z (2018) Functional polymer surfaces for controlling cell behaviors. *Mater Today* 21:38–59

37. Raja IS, Fathima NN (2014) Porosity and dielectric properties as tools to predict drug release trends from hydrogels. *Springerplus* 3:393
38. Srikanth M, Asmatulu R, Cluff K, Yao L (2019) Material characterization and bioanalysis of hybrid scaffolds of carbon nanomaterial and polymer nanofibers. *ACS Omega* 4:5044–5051
39. Raja IS, Lee SH, Kang MS, Hyon SH, Selvaraj AR, Prabakar K, Han DW (2022) The predominant factor influencing cellular behavior on electrospun nanofibrous scaffolds: wettability or surface morphology? *Mater Design* 216:110580–110590
40. Fadaie M, Mirzaei E, Geramizadeh B, Asvar Z (2018) Incorporation of nanofibrillated chitosan into electrospun PCL nanofibers makes scaffolds with enhanced mechanical and biological properties. *Carbohydr Polym* 199:628–640
41. Li Y, Yu Z, Ai F, Wu C, Zhou CC, Li W (2021) Characterization and evaluation of polycaprolactone/hydroxyapatite composite scaffolds with extra surface morphology by cryogenic printing for bone tissue engineering. *Mater Design* 205:109712–109720
42. More N, Srivastava A, Kapusetti G (2020) Graphene oxide reinforcement enhances the piezoelectric and mechanical properties of poly(3-hydroxybutyrate-co-3-hydroxy valerate)-based nanofibrous scaffolds for improved proliferation of chondrocytes and ECM production. *ACS Appl Bio Mater* 3:6823–6835
43. Pan L, Pei X, He R, Wan Q, Wang J (2012) Multiwall carbon nanotubes / polycaprolactone composites for bone tissue engineering application. *Colloids Surf B Biointerfaces* 93:226–234

ABSTRACT(IN KOREAN)

**상처 치유 및 피부 재생을 촉진하는 활성탄소 나노섬유 함유
전기방사 폴리카프로락톤 지지체**

<지도교수 박종철>

연세대학교 대학원 의공학학과

최 상 문

조직공학에서 가장 널리 사용되는 일차원 (1D) 탄소성 나노물질은 탄소 나노튜브인데, 이는 단일 벽 또는 다중 벽 형태로 존재한다. 다른 형태의 1D 나노물질로는 탄소 나노와이어와 탄소 나노섬유가 있으나, 이들은 생의학 응용 분야에서 덜 연구되었다. 본 연구에서는 폴리아크릴로니트릴 (Polyacrylonitrile)로 만든 전기방사 나노섬유로부터 안정화, 알칼리 처리, 열분해 및 연삭과 같은 연속적인 과정을 통해 1D-활성화된 탄소 나노섬유 나노입자(Activated Carbon Nanofiber Nanoparticles, ACNF NPs)를 합성하였다. 두 가지 다른 유형의 ACNF NPs 를 포함하는 전기방사 폴리카프로락톤 (Polycaprolactone, PCL) 나노섬유 매트, 즉 표면을 수정한 NP 가 첨가된 매트 (ACNF@PCL)와 NP 가 포함된 매트 (ACNF-PCL)를 준비하여 그들의 피부 조직공학 지지체로서의 잠재력을 검토하였다. 라만 분광학 결과 ACNF NPs 가 그래핀화 정도를 보임을 확인하였으며, 이의 ID/IG 비율은 1.05 였다. 스캐닝 전자 현미경 (Scanning Electron Microscopy, SEM)

관찰 결과 ACNF NPs 의 지름은 평균적으로 280 ± 100 nm, 길이는 565-3322 nm 범위였다. NP 농도가 30 $\mu\text{g}/\text{mL}$ 이상일 경우, 48 시간 동안 NIH3T3 섬유아세포의 생존률이 70% 미만으로 독성을 나타내었다. 그러나 ACNF-PCL 나노섬유 매트는 1, 3, 5 일 동안 PCL 및 ACNF@PCL 매트와 비교하여 더 나은 세포 증식 성능을 보였다. 이러한 결과를 바탕으로, ACNF NPs 의 농도가 낮은 ACNF-PCL 매트는 세포 성장을 더욱 효과적으로 지원할 수 있으며, 이는 피부 조직의 재생에 중요한 영향을 미칠 것으로 예상된다.

핵심되는 말 : 전기방사 나노섬유, 활성화된 탄소 나노섬유 나노입자, 폴리카프로락톤, 피부 조직공학